

A Self-Moving Piezoelectric Actuator With High Carrying/Positioning Capability via Bending-Resonant-Vibration-Induced Stick-Slip Motion

Jinshuo Liu^{ID}, Zhaochun Ding^{ID}, Jiang Wu^{ID}, Lipeng Wang^{ID}, Teng Chen^{ID}, Xuewen Rong^{ID}, Rui Song^{ID}, *Member, IEEE*, and Yibin Li^{ID}

Abstract—A self-moving piezoelectric actuator (SMPA) with high carrying/positioning capability is presented in this article. Its Π -shaped mechanical part comprises four piezo-legs, each of which combines the bending vibrations in the first three orders into the motion in the quasisawtooth waveform at the driving foot. Besides, a homemade onboard circuit is integrated with the mechanical part to form compact structure. Initially, by establishing a Krimhertz-transmission-theory-based model, the piezo-leg's resonant frequencies of the 1st, 2nd, and 3rd bending modes were structurally tuned to be approximately 1:2:3. Subsequently, a prototype with the size of $75 \times 55 \times 55 \text{ mm}^3$ and the weight of 38.5 g was fabricated to assess its moving/carrying/positioning performance. At 2065 Hz frequency, SMPA in a tethered manner yielded the maximal payload of 1130 g (equal to 29.3 times of its weight), the maximal speed of 224.1 mm/s, and the maximal towing force of 1.24 N. In an untethered manner, SMPA provided planar movements when receiving the command wirelessly, and it produced the minimal step displacements and the maximal running distance of 12.2 nm and 9.16 m, respectively. Benefiting from the two-DOF untethered movement, SMPA is potentially applicable to the robotic-assistant precise operation, e.g., cell puncture.

Index Terms—Bending resonant vibration-induced stick-slip motion, high carrying capability, nanometer resolution, piezoelectric actuator (PA).

Manuscript received 10 April 2024; revised 22 June 2024; accepted 11 July 2024. This work was supported in part by the National Natural Science Foundation of China (NSFC) under Grant 52105029, in part by the Science Center Program of NSFC under Grant 62188101, in part by the Natural Science Foundation of Shandong Province under Grant ZR2021QE020, in part by the Foundation of Taishan Scholar Project under Grant tsqn202306052, and in part by Shandong Provincial Major Scientific and Technological Innovation Project under Grant 2021CXGC011207. (Jinshuo Liu and Zhaochun Ding are co-first authors.) (Corresponding authors: Jiang Wu; Xuewen Rong; Rui Song; Yibin Li.)

The authors are with the School of Control Science and Engineering, Shandong University, Jinan 250061, China (e-mail: liujinshuo@mail.sdu.edu.cn; dingzhaochun@mail.sdu.edu.cn; wujiang@sdu.edu.cn; 202220715@mail.sdu.edu.cn; chenteng100@sdu.edu.cn; rongxw@sdu.edu.cn; rsong@sdu.edu.cn; liyb@sdu.edu.cn).

This article has supplementary material provided by the authors and color versions of one or more figures available at <https://doi.org/10.1109/TIE.2024.3429612>.

Digital Object Identifier 10.1109/TIE.2024.3429612

1. INTRODUCTION

PIEZOELECTRIC actuators (PAs) offer simple structure [1], [2], quick response [3], [4], and absence of electromagnetic (EM) interference [5], [6] compared with EM motors and they provide the basic technique in some specific fields, e.g., precise operation/manipulation [7], [8], microelectromechanical system [9], [10], or miniature robots [11], [12]. To accelerate practical application in these fields, currently, PAs' development concentrates on the following aspects. First, the carrying capability should be satisfactorily high as the functional components (e.g., needles, mirrors, or lens) are necessarily arranged onto PAs [11], [13]. Second, small step displacements within large strokes are needed for precise operation/manipulation [14], [15]. Third, the approach to accomplish the untethered movement deserves the exploitation as it can enlarge PAs' movable ranges [16], [17].

In general, PAs operate by the following principles: ultrasonically actuating, directly driving, inchworm, and stick-slip. Ultrasonic actuators (or motors) employ resonant vibration in the ultrasonic frequency range ($>20 \text{ kHz}$) to drive the sliders (or rotors), and they provide good mechanical output but insufficient resolution [18]. For instance, Li et al. [19] devised a standing-wave-type PA with 300 g payload and $0.25 \mu\text{m}$ resolution. Wu et al.'s traveling-wave-type PA [18], where the lead-zirconate-titanate (PZT) disks were clamped with the rectangular blocks, provided 66 mm/s speed and $2.4 \mu\text{m}$ resolution. Li et al.'s seal-inspired PA [17] had the maximal speed of 146 mm/s. As the commercially-available amplifiers/MOSFETs have insufficient bandwidths, it is still challenging to design small-sized onboard circuits at the ultrasonic frequency range [1]. In contrast, the directly-driving PAs work in the non-resonant vibration. Guan et al. [20] used a spool-driving mechanism that was not fully in contact with piezoelectric stacks (PSs) to form a servo valve, whose strength was, however, limited by PSs' fragility. The inchworm PAs use several groups of PSs in orthogonal legs to achieve the step-by-step movements [21], [22]. For example, Ma et al. [23] designed a cubic PA capable of climbing the pillar and obtained 85 nm resolution. Despite high precision, inchworm PAs are complex in structure and control strategy [24]; this increases the technical difficulty in integrating the mechanical and electrical systems. The stick-slip PAs

use the slowly-extending and quickly-contracting motions of piezoelectric transducers or PSs to push the sliders [25]. Wang et al.'s skateboard-inspired PA [26] had 45 nm resolution and 200 g payload (17.5 times its weight). Inspired by the biped structure of human beings, Li et al. [27] devised a pair of L-shaped actuators with 84 nm resolution and 1100 g payload (12.2 times its weight). The stick-slip principle facilitates simple structure and precise movement of PAs [28], but the nonresonant state unavoidably restricts the mechanical output (e.g., the speed) [1], [12]. Besides, since PSs comprise multilayered ultrathin PZT plates, their clamped capacitances (in the order of μF) require that the onboard circuits use the transistors/amplifiers in large profiles as their currents and slew rates are high enough for actuation [29]. These discussions imply that good carrying/positioning performance and untethered movement are not easy to achieve on condition that PAs adopt only one principle.

To tackle this problem, PAs can be driven by combining two (or more) principles [30]. The first way is to independently apply the waveforms corresponding to multipinciples (e.g., sine or sawtooth wave) to single PA [31]. For example, Li et al. [32] used three inertial impact vibrations to form a miniature PA with 24.8 mm/s speed and 0.5 μm resolution. Direct combination of multipinciples enriches the variety in motions, but it makes PAs not easy to design as a certain configuration is, in most cases, not optimal for multipinciples. The second way is to excite the intermittent vibration in the quickly-contracting period to improve the stick-slip PA's stability [33], but the usage of additional power supplies is not desirable in terms of integration [34]. The third way is that the inchworm or stick-slip motions of PAs can be formed by exciting the resonant vibrations. As an instructive example, Deng et al. [24] used dual vibrations in radially-expanding and longitudinal modes with a dumbbell-shaped transducer to form an inchworm PA with 0.71 μm resolution. Morita et al. [35] combined the 1st and 3rd longitudinal vibrations to obtain the motion in a sawtooth waveform at 288 kHz frequency with one PS. Wang et al. [36] followed this principle but replaced a PS with a clamped-type longitudinal transducer. Actually, the stick-slip motion induced by the longitudinal vibration is not suitable for self-moving PAs as a consequence of their large profiles (particularly along the moving direction), but the approach to synthesize the sawtooth waveform is interesting as it potentially inherits the merits of both the resonant vibration and the stick-slip motion. Besides, in this situation, the current has the function of exciting the resonant vibration instead of charging the clamped capacitance [24]; this somewhat lowers the requirement in the performance of small-sized amplifiers (e.g., the bandwidth or the slew rate), desirable for achieving PAs' untethered movements.

In this article, a self-moving PA (SMPA) with high carrying/positioning capability is developed by generating the bending-resonant-vibration-induced stick-slip motion. Concerning the configuration, four hollow-shaped piezo-legs are bonded onto an alumina plate to form a Π -shaped actuator. Here, alumina's high rigidity can suppress the vibration interference among the piezo-legs [29]. Regarding the operating principle, the resonant frequencies of the 1st, 2nd, and 3rd bending vibrations of the

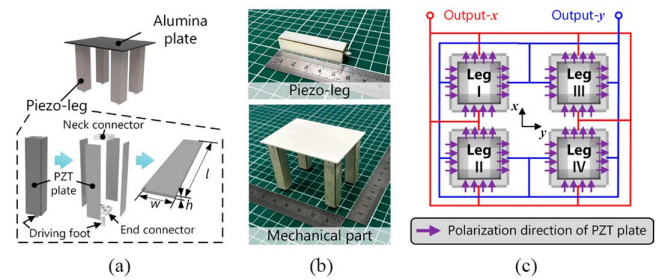


Fig. 1. Basic configuration of SMPA. (a) Π -shaped mechanical part composed by four piezo-legs and an alumina plate. Here, each piezo-leg is formed by bonding four PZT plates onto two connectors. (b) Photos of single piezo-leg and the mechanical part. (c) Polarizing directions of the PZT plates and their connection with the electrical ports (Fig. 8 for the output-x and the output-y).

piezo-legs are structurally tuned to nearly 1:2:3 (corresponding to the frequency ratio of the first three peaks in the sawtooth wave's spectrum [3]) to achieve the stick-slip motion at the driving foot. Note that the 1:2:3 ratio is structurally difficult to achieve for conventional longitudinal transducers or PSs as the resonant frequencies are prominently determined by the lengths [37], while the bending vibration of the piezo-legs, whose resonant frequencies are affected by various dimensions, endows the flexibility in tuning the resonant frequencies [38]. Besides, an onboard circuit that not only actuates the mechanical part but also has carryable weight and small size is designed to guarantee SMPA's untethered movements.

Benefiting from the technical features of bending-resonant-vibration-induced stick-slip actuation and compact integration between vibration and electrical systems, SMPA possesses the following specifications.

- 1) The mechanical part has the size of $75 \times 55 \times 55 \text{ mm}^3$ and the weight of only 38.5 g.
- 2) In a tethered manner, SMPA yields the maximal speed of 224.1 mm/s and the maximal payload of 1130 g (equal to 29.3 times of its own weight). Besides, its maximal towing force is 1.24 N, corresponding to the towing force density of 32.2 N/kg.
- 3) SMPA accomplishes an untethered movement with the minimal step displacement of 12.2 nm. Installed with a battery with 7.4 V voltage and 350 mAh capacity, SMPA produces the running distance of 9.16 m.

The rest of this article is organized as follows. Section II introduces the configuration, operating principle, modeling, and design. Sections III and IV show its moving/carrying/positioning performance in tethered and untethered manners, respectively. Section V demonstrates its potential application to cell puncture. Section VI concludes this article.

II. DESIGN OF SMPA

A. Basic Configuration

Fig. 1(a) illustrates SMPA's mechanical part, whose four piezo-legs are mounted onto an alumina plate. Each piezo-leg in the hollow shape contains four pieces of PZT plates (P5H, Shenlei Corp., Zhejiang, China), two duralumin connectors, and a

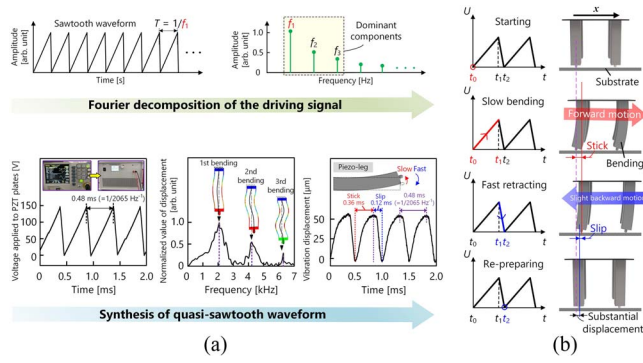


Fig. 2. Operating principles of (a) a piezo-leg and (b) SMPA.

driving foot. The PZT plate has the thickness (h) of 0.5 mm for the cost-efficiency, while the length (l) and the width (w) are discussed later. The PZT plates' fixed ends are bonded onto the neck connector, while their free ends are bonded with the end connector. A pin is inserted into the end connector's central hole to form the driving foot. Fig. 1(b) gives the photograph of single piezo-leg and the mechanical part. Fig. 1(c) shows the PZT plates' polarizing directions as well as their connections with the electrical ports. Taking two pieces of parallel-arranged PZT plates in a piezo-leg as an example, the polarizing directions are identical, while the external electrodes are connected with one electrical port and the internal ones with the ground. In this case, these two PZT plates produce the out-of-phase longitudinal vibrations, which cause the piezo-leg to vibrate in a bending mode. Moreover, the piezo-legs have the same arrangements in the polarizing directions. For the x -axis movement, the voltage applied to the front piezo-legs (I and III) is simultaneous with that to the back ones (II and IV), while for the y -axis movement, the voltage applied to the piezo-legs I and II is simultaneous with that to the piezo-legs III and IV.

B. Operating Principle

- 1) *Stick-slip motion of a piezo-leg.* Based on the sawtooth wave's spectrum [Fig. 2(a)], the first three components are dominant as their magnitudes are larger than the higher-order components. Accordingly, a quasi-sawtooth waveform can be obtained when the resonant frequencies of the 1st, 2nd, and 3rd bending vibrations (f_1 , f_2 , and f_3) equal $\sim 1:2:3$ as the first three components have identical intervals in the frequency domain (essentially, the piezo-leg acts as the bandpass filters with triple central frequencies). Fig. 2(b) illustrates the synthesis of the quasi-sawtooth wave. In the case that a sawtooth signal with the fundamental frequency (i.e., f_1) of 2065 Hz is applied, the 1st, 2nd, and 3rd bending vibrations exist on the piezo-leg, and their superposition enables the driving foot to oscillate in a quasisawtooth waveform, which leads to the stick-slip motion at $f_1 = 2065$ Hz.
- 2) *Operating principle of entire SMPA.* Fig. 2(b) illustrates SMPA's stick-slip movement, which can be divided into starting, slow bending, fast retracting, and re-preparing states.

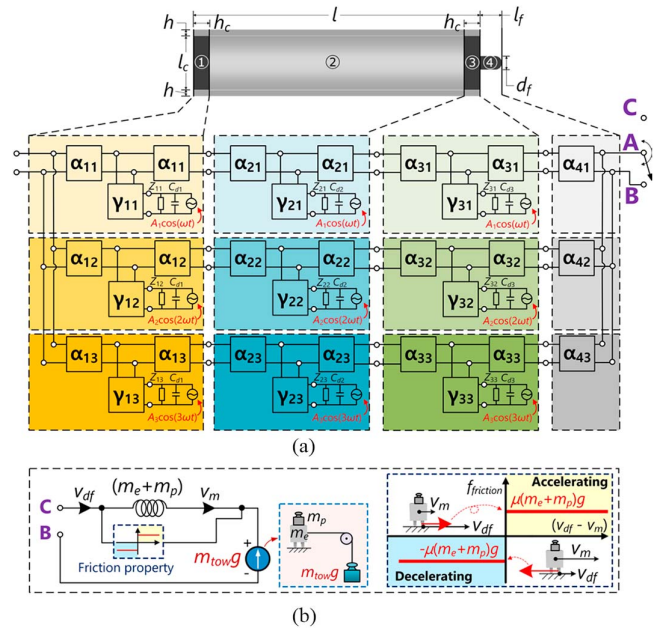


Fig. 3. (a) Krimhertz-transmission-theory-based model for analyzing the vibration properties and (b) model for analyzing the carrying/towing performance. When the ports are connected in the sequence of A→B, the resonant frequencies of the Piezo-legs' bending vibrations can be estimated. When the connection is switched to A→C→B, the model can be used to analyze how the payload and towing force affect the speed.

Stage I (t_0): When the voltage applied to the PZT plate is zero, SMPA locates in the starting state.

Stage II (t_0-t_1): The gradual enhancement in the voltage causes the piezo-legs to produce the slowly-bending motion, allowing both the piezo-legs' upper parts and the alumina plate to move in the forward direction, while the driving feet remain at their original positions.

Stage III (t_1-t_2): The rapid reduction in the voltage induces the fast-retracting deformation, causing the slippery between the driving feet and the ground. Though the upper parts and the alumina plate slightly provide the backward movement, the actuator entirely moves in the forward direction.

Stage IV (t_2): The piezo-legs return to the undeformed condition and prepare the stick-slip motion in the next period.

By repeating the stages from I to IV, SMPA provides the forward movement. Whereas it moves in the backward direction when the piezo-legs provide the rapidly-bending and slowly-retracting motions in stages II and III, respectively.

C. Modeling and Design

- 1) *Establish a Krimhertz-transmission-theory-based model.* Fig. 3(a) illustrates part of the model for analyzing the vibration properties when its right side is in short connection. Concerning the architecture, the model has three branches that represent the 1st, 2nd, and 3rd bending vibrations. Each branch comprises four serially-connected blocks, which correspond to the neck connector, hollow part, end connector, and driving foot. In each block, several elements exist in T shapes, standing for the wave propagation and/or the electromechanical

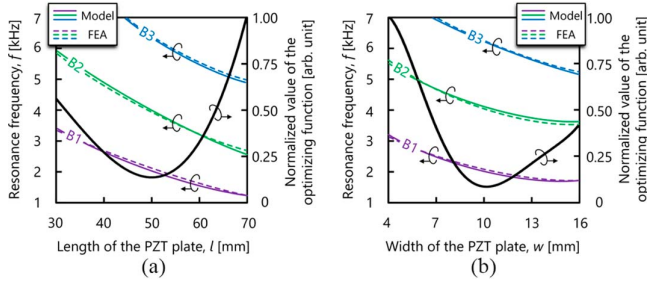


Fig. 4. Resonant frequencies and the normalized values of optimizing function as functions of (a) PZT plate's length and (b) width. Here, B1, B2, and B3 are respectively the 1st, 2nd, and 3rd bending vibrations. Besides, the results calculated by the model (indicated as the solid curves) coincide with those from the finite element analysis (FEA) (the dashed curves). The values of the optimizing function are derived from the results calculated by the model (the solid curves).

coupling properties. Regarding the boundary condition, the external ports in the left side are in the open states as the neck connector is bonded onto the alumina plate. After building the model in Simulink, we calculate f_1 , f_2 , and f_3 by the frequency-sweep method [39].

By switching the right side, the portion representing the friction property, as shown in Fig. 3(b), is included to analyze how the payload and/or the towing force affect the speed. Here, the friction force alters its direction according to the discrepancy between the vibration velocity at the driving foot and the actuator's speed [4]. Meanwhile, the towing force is modeled as a DC voltage source. The elements' definitions are given in Appendix A.

- 2) *Decide the key dimensions.* As the values of f_2 and f_3 are, as mentioned above, twice and third that of f_1 , respectively, an optimizing function is set as follows:

$$F = \frac{\lambda_1 \cdot |f_2 - 2f_1| + \lambda_2 \cdot |f_3 - 3f_1|}{f_1} \quad (1)$$

where λ_1 and λ_2 are set to 0.75 and 0.25, respectively [40]. It can be found in Fig. 4(a) and 4(b) that the optimization function reaches the minimal values at $l = 50$ mm and $w = 11$ mm, so we set these values as the PZT plate's dimensions. In this case, f_1 , f_2 , and f_3 equal 2065, 4145, and 6283 Hz, respectively, where f_1 is chosen as the working frequency f .

III. MOVING/CARRYING/TOWING PERFORMANCE IN A TETHERED MANNER

A. Moving Performance

First, SMPA's movements on a glass floor (whose Young's modulus and shear modulus were 71.7 and 29.9 GPa, respectively [41], [42]) were explored when f and the driving voltage V were varied. The voltage was applied with the amplifiers (5052, Agitek, Xi'an, China), while the speed was measured with a speed meter (HG-200, Aero-top, Hitech Corp., Beijing, China). Fig. 5(a) illustrates that the peak speed of 224.1 mm/s exists at $f = 2065$ Hz when SMPA moves along the x axis.

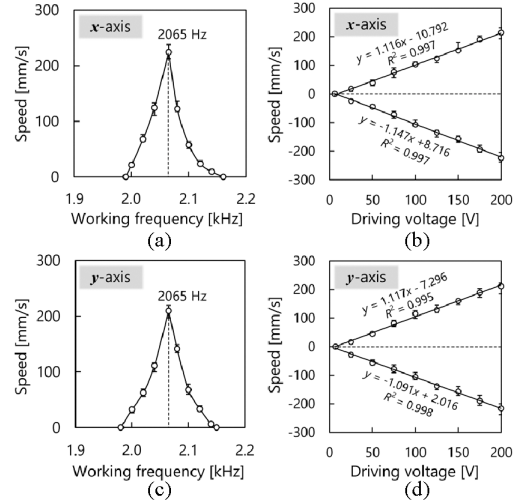


Fig. 5. Moving performance. The x -axis speed as functions of (a) working frequency and (b) driving voltage. The y -axis speed as functions of (c) working frequency and (d) driving voltage. (b) and (d) Working frequencies were set to 2065 Hz.

Fig. 5(b) plots that, at 2065 Hz, the speed increased in a nearly linear manner with increasing V . When SMPA moved along the y axis, the speed reached 209.5 mm/s at 2065 Hz [Fig. 5(c)]. Fig. 5(d) shows how the y -axis speed is related to V ; this is similar to the relationship for the x -axis movement.

B. Straightness of Movement

Next, the straightness was evaluated in terms of SMPA's movement. Fig. 6(a) shows a series of photos of SMPA's positions in the x -axis movement. Fig. 6(b) plots the central point's positions at the speed of ~ 50 mm/s. It can be found that the fitting line slightly deviates from the predicted trajectory (strictly along the x axis) by 1.05° and the error is in the range from -0.7 to 5.5 mm. Fig. 6(c) illustrates that, at ~ 150 mm/s, the deviating angle and the error band do not exceed 3.52° and 16.4 mm, respectively. For the y -axis movement [Fig. 6(d)], the deviating angle and the error at ~ 50 mm/s do not markedly differ from those for the x -axis movement [Fig. 6(e)]. Whereas the maximal deviating angle and the maximal error band are 4.41° and 16.7 mm, respectively [Fig. 6(f)]. These results demonstrate SMPA's capability to provide nearly straight movement.

C. Carrying and Towing Performance

Then, SMPA's payloads and towing forces were measured to assess the carrying/towing capability. Here, V and f were set to 200 V and 2065 Hz, respectively. Fig. 7(a) shows how the x -axis speed changes with varying payload. Clearly, the speed became larger in a gradual way with increasing payload. The maximal payload reached 1130 g, equal to 29.4 times the weight of the mechanical part. The theoretical results also show the tendency of gradual decrease, but they slightly exceed the experimental results dominantly because of the vibration reduction [18]. Fig. 7(b) illustrates the x -axis speed as functions of the towing force at different payloads. At 200 g payload, the speed decreased from 203.9 to 9.9 mm/s when the towing force

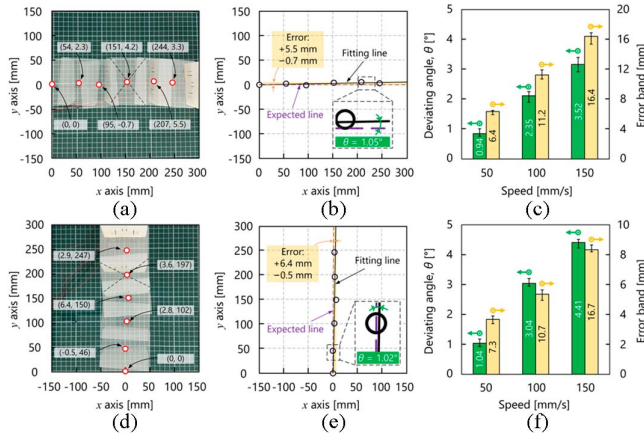


Fig. 6. Evaluation of the straightness of SMPA's planar movement. (a) Position and (b) fitting line and the error of the x-axis movement, as well as (c) deviating angles and error bands at the x-axis speed of 50, 100, and 150 mm/s. (d) Position and (e) fitting line and the error of the y-axis movement as well as (f) deviating angles and the error bands at the y-axis speed of 50, 100, and 150 mm/s.

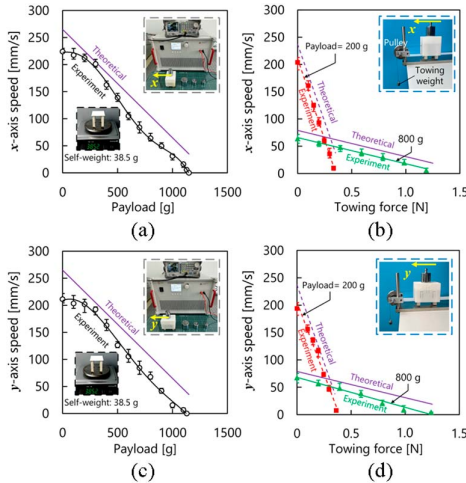


Fig. 7. Carrying and towing performance. The x-axis speed as functions of (a) payload and (b) towing force as well as the y-axis speed as functions of (c) payload and (d) towing force. The theoretical results obtained by the model and the experimental ones are indicated as the curves in purple and the other colors, respectively.

increased from 0 to 0.33 N. When the payload increases to 800 g, SMPA yielded the maximal towing force of 1.19 N. As shown in Fig. 7(c), SMPA carried 1100 g payload for the y-axis movement. Fig. 7(d) illustrates that, compared with the x-axis movement, the towing performance of the y-axis movement does not show observable difference except the relatively high towing force of 1.24 N.

IV. MOVING/POSITIONING PERFORMANCE IN AN UNTETHERED MANNER

A. Onboard Circuit

Initially, an onboard circuit was designed to guarantee the untethered movement and its schematic was shown in Fig. 8(a). Concerning the controlling circuit, after it wirelessly receives

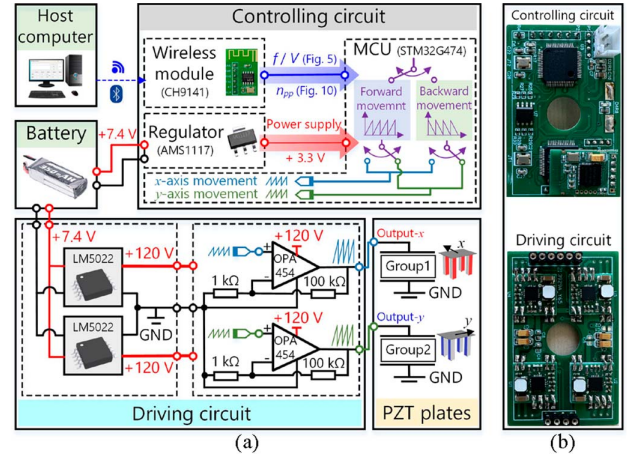


Fig. 8. Onboard circuit's. (a) Schematic and (b) photographs.

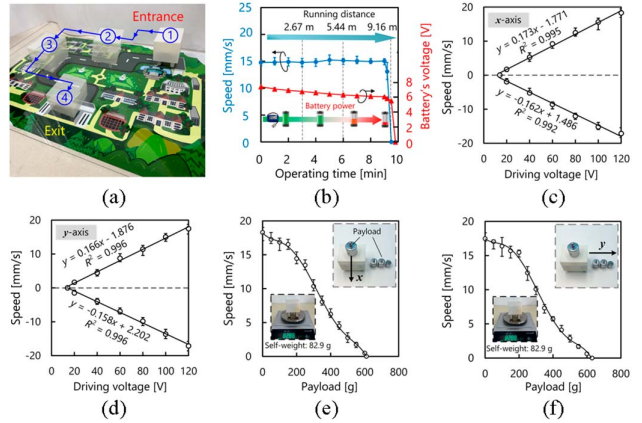


Fig. 9. Untethered movement in continuous operation: (a) demonstration of the movement on a map; (b) variations in the speed and the battery's voltage in the time domain; (c) x-axis speed; (d) y-axis speed as functions of the working voltage; (e) x-axis speed; and (f) y-axis speed as functions of the payload.

the commands from a host computer, the microcontroller unit (MCU) produces the signals. In specific, the x- or y-axis movement determines which channel(s) of voltage is applied, the forward or backward movement in a certain axis decides the waveform (i.e., slowly or rapidly enhancement in stage II), the results given in Fig. 5 determines that $f = 2065$ Hz, and the target speed decides V (according to the relationship given in Fig. 9). Regarding the amplifying circuit, first, the voltage provided with a 7.4-V 350-mAh lithium battery is boosted to 120 V with the boost modules (LM5022, TI Corp., Dallas, USA). Then, the signals produced with the controlling circuit are amplified with the amplifiers (OPA454, TI Corp., Dallas, USA) to drive the piezo-legs [Fig. 1(c)]. Fig. 8(b) shows the photos of the controlling and driving circuits.

B. Continuous Operation

Subsequently, SMPA's movement was tested in continuous operation. During the movement on a map [Fig. 9(a)], it achieved two-DOF translational movements and arrived at the

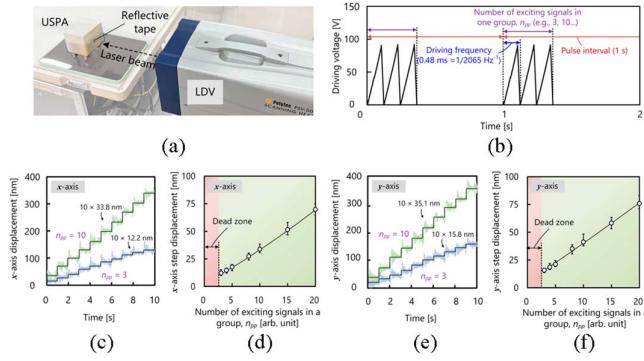


Fig. 10. Untethered movement in stepping operation: (a) testbed; (b) applied voltage; (c) x-axis displacement in the time domain; (d) x-axis step displacement as functions of the number of exciting signals; (e) y-axis displacement in the time domain; and (f) y-axis step displacement as functions of the number of exciting signals.

exit. As shown in Fig. 9(b), the maximal operating time was ~ 9.5 min at an average speed of 15 mm/s and the stroke was 9.16 m (note that the stroke of the untethered actuator stood for the maximal running distance supported with single battery; this differed from the tethered actuator's stroke as it was commonly limited by the slider's length or the mechanism [13]). Besides, during this test, SMPA moved in a reciprocating way while the battery's output voltage was monitored. When the voltage fell down to 5.8 V at 9.2 min, SMPA stopped running sharply as this voltage could not support normal operation of the electrical components (e.g., the transistor or the MCU).

By using the speed meter, SMPA's speeds were measured at different V s. Fig. 9(c) shows the relationships between the speed and V . The speeds reached 18.3 and 17.5 mm/s in the $+x$ and $-x$ axes, respectively. Fig. 9(d) shows how the speed depends on V for the y -axis movement. The above relationships provide the basis for deciding V in the controlling circuit. Fig. 9(e) shows how the speed changes with varying payload for the x -axis movement at $f = 2065$ Hz and $V = 120$ V. SMPA yielded the maximal payload of 610 g. Similar tendency can be found for the y -axis movement [Fig. 9(f)] except the maximal payload of 630 g, equal to 7.6 times the weight of entire SMPA.

C. Stepping Operation

Followingly, SMPA's movements were explored in stepping operation. As shown in Fig. 10(a), a laser Doppler vibrometer (PSV-500, Polytec, Waldronn, Germany) was used to measure the displacement. f and V followed the values in the former section. Fig. 10(b) illustrates that the pulse contains many groups of sawtooth exciting signals (whose number in one group n_{pp} is changeable) and the interval between adjacent groups is set to 1 s. As shown in Fig. 10(c), at $n_{pp} = 3$, the x -axis step displacement reached 12.2 nm, indicating SMPA's high positioning capability. Fig. 10(d) illustrates that, at $n_{pp} \geq 3$, the step displacement increases gradually as n_{pp} becomes larger. For the y -axis movement, the minimal step displacement is 15.8 nm [Fig. 10(e)] and the increasing tendency can be also found in Fig. 10(f). Moreover, the stroke (9.16 m) is 7.5×10^8 times the minimal step displacement in the x axis; this implies SMPA's cross-scale moving capability.

D. Performance Comparison

Finally, SMPA's performance was compared with those of several typical PAs. The results listed in Table I imply that the following items.

- 1) Though the stick-slip principles are adopted in SMPA and Wang et al.'s actuator [12], a relatively high payload-to-weight ratio is produced with SMPA as its stick-slip motion is induced by a powerful actuating approach [18], namely the resonant vibration [43].
- 2) Hariri et al.'s inchworm actuator has extremely small thickness [44], but the phased signals are needed to generate the movement in single direction; this increases the complexity in structure and consequently causes its payload-to-weight ratio to be 0.15 times that of SMPA despite that both of them work in tethered manners.
- 3) Since Wei et al.'s actuator [29] uses polyphenylene sulfide (PPS), an engineering polymer, as the transducer's basic material, its speed is larger than that of SMPA for PPS's low density [45]. However, its payload-to-weight ratio is 0.29 times the value of SMPA in an untethered manner for PPS's low stiffness [45]. Besides, the positioning capability of Wei et al.'s actuator is not superior to SMPA possibly because the linear region of the stress-strain relationship is limited for PPS [46].
- 4) Li et al.'s actuator [32], which independently utilizes the diagonal, jumping, and resonant vibrations, provides an idea to obtain balanced performance of PAs. However, as the main body should provide specific motions (e.g., the tiny motion or the resonant vibration), it is challenging to develop the structure suitable for various principles; this may be mitigated by using the bioinspired structure based on multiple appendages [47].
- 5) When the actuator adopts a stepping manner, the exciting signals should be precise to guarantee the positioning capability [39]; this is, to a certain extent, easier for the onboard circuit than for the large-sized power supply as the latter easily has the cut-off distortion [48]. It is assumed as a reason for larger step displacement for Deng et al.'s actuator [24] than for SMPA.

These comparisons demonstrate high carrying/positioning capability of SMPA, implying its potential applicability as an essential hardware for the robotic-assistant precise operation.

V. POTENTIAL APPLICATION TO CELL PUNCTURE

A preliminary investigation was conducted to test SMPA's potential application to cell puncture, where the robotic-assistant operation was in great demand to reduce the labor cost [49]. Fig. 11(a) shows the experimental setup. An injecting pipette was mounted onto SMPA and its tip's position was adjusted to achieve the two-DOF movement and the injection. Several zebrafish embryos were arranged in the slots, and their positions were monitored with an industrial camera (MV-CE200-10GC, HIKVISION, Hangzhou, China). As shown in Fig. 11(b), initially, the tip approached the embryo orthogonally to the slot and punctured into the embryo at the instant that it was in contact with the cell membrane. Subsequently, SMPA

TABLE I
PERFORMANCE COMPARISON BETWEEN SMPA AND SEVERAL TYPICAL PAS

	This Study	Wang et al. [12]	Hariri et al. [44]	Wei et al. [29]	Li et al. [32]	Deng et al. [24]
Operating principle	Resonant-vibration-induced stick-slip motion	Conventional stick-slip	Conventional inchworm	Conventional resonant vibration	Combining three inertial impact vibrations	Resonant-vibration-induced inchworm motion
Profile	Four piezo-legs in Π shape	Dual patch-type beam shape	Thin plate shape	Dual-block shape	Rectangular shape	Dumbbell shape
Dimension [mm ³]	75 × 55 × 55 (mechanical body) 80 × 60 × 80 (entire SMPA)	39 × 15 × 4 (mechanical body) 56 × 35 × 28 (entire actuator)	180 × 60 × 0.95 (only mechanical body)	46 × 24 × 10 (mechanical body) 49 × 45 × 30 (entire actuator)	20 × 12 × 9 (only mechanical body)	65 × 30 × 30 (only mechanical body)
Weight [g]	38.5 (mechanical body) 82.9 (untethered SMPA)	0.9 (mechanical body) 11.9 (untethered actuator)	20.4 (only mechanical body)	53.4 (untethered actuator)	4.7 (only mechanical body)	56.7 (only mechanical body)
DOF	2	2	2	1	1	1
Tethered / untethered	Tethered and untethered	Untethered	Tethered	Untethered	Tethered	Tethered
Working frequency	2065 Hz	130 Hz	11200 Hz	1648 Hz	1510 Hz	21500 Hz
Minimal step displacement	12.2 nm	NA	NA	31.9 nm	500 nm	710 nm
Maximal payload	1130 g (tethered) 630 g (untethered)	12.5 g	90 g	117 g	31.3 g	NA
Payload-to-weight ratio	29.3 (tethered) 7.6 (untethered)	1.1	4.4	2.2	6.7	NA
Maximal speed	224.1 mm/s	1.3 mm/s	133.3 mm/s	231.6 mm/s	24.8 mm/s	200 mm/s

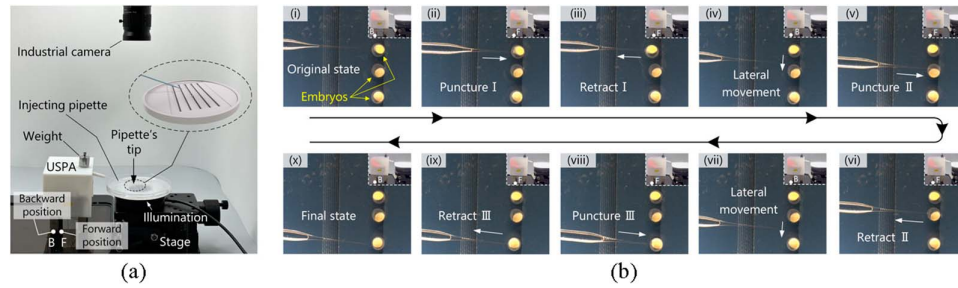


Fig. 11. SMPA's potential application to cell puncture. (a) Experimental setup and (b) sequence of photos showing the process.

caused the tip to retract from the embryo; this process changed the embryo's position possibly because of the dragging force between the pipette and the membrane. Followingly, SMPA moved in the lateral direction to the next embryo, and finally, it completed the process (see the supplementary video); this demonstrates SMPA's potential for cell puncture owing to the untethered two-DOF movements.

VI. CONCLUSION

This article presented the proposal, design, and performance assessment of SMPA. Through numerical analysis and experimental investigation, we have drawn these conclusions.

- 1) SMPA with high carrying/positioning capability was developed via the bending resonant vibration-induced stick-slip motion.
- 2) A Krimhertz-transmission-theory-based model was built to structurally tune the resonant frequencies of the 1st, 2nd, and 3rd bending vibration to generate the stick-slip motion.
- 3) In a tethered manner, SMPA yielded the maximal speed of 224.1 mm/s, the maximal payload of 1130 g (equal to

29.3 times of its weight), and the maximal towing force of 1.24 N (corresponding to the towing force density of 32.2 N/kg).

- 4) SMPA accomplished the untethered movement according to the wireless command and its minimal step displacement and stroke reached 9.16 m and 12.2 nm, respectively.
- 5) SMPA exhibited the potential application to cell puncture owing to the two-DOF untethered movement.

These conclusions not only validate the effectiveness of our proposal but also provide a new way to design the untethered PAs. In the future, we will focus on promoting the philosophy to design the electronic systems and the assembly method prior to SMPA's practical application.

APPENDIX A: DEFINITIONS OF ELEMENTS IN MODEL

A. Elements for Analyzing the Vibration Property

The elements given in Fig. 3(a) are defined according to the piezo-leg's configuration, dimensions, material constants, and vibration modes, and they are given as follows.

1) *Neck connector*. The matrix α_{1i} denotes the property of the wave propagation when the neck connector works in the i th bending vibration ($i = 1, 2$, and 3) [50], [51] where j is the imaginary unit, f_i is the resonant frequency of the i th bending vibration, l_c and h_c are respectively the neck connector's length and height (Fig. 3), l and h are (as mentioned in Section II), respectively, the PZT plate's length and thickness, ρ_p ($7.8 \times 10^3 \text{ kg/m}^3$) is the density of PZT, C_{11} (145 GPa) is the Young's modulus of PZT orthogonal to the polarizing direction, ρ_{AL} ($2.7 \times 10^3 \text{ kg/m}^3$) is duralumin's density, and E_{AL} (70.3 GPa) is duralumin's Young's modulus.

The matrix γ_{1i} and the impedance Z_{1i} , both of which stand for the electromechanical coupling properties of the neck connector, are expressed as [50], [51]

$$\gamma_{1i} = \begin{bmatrix} 0 & -j \cdot \frac{h\rho_p^{\frac{1}{2}}C_{11}^{\frac{1}{2}}}{2e_{31}\sin\left(\pi f_i h_c \rho_p^{\frac{1}{2}}C_{11}^{-\frac{1}{2}}\right)} \\ -j \cdot \frac{2e_{31}\sin\left(\pi f_i h_c \rho_p^{\frac{1}{2}}C_{11}^{-\frac{1}{2}}\right)}{h\rho_p^{\frac{1}{2}}C_{11}^{\frac{1}{2}}} & 0 \end{bmatrix} \quad (\text{A2})$$

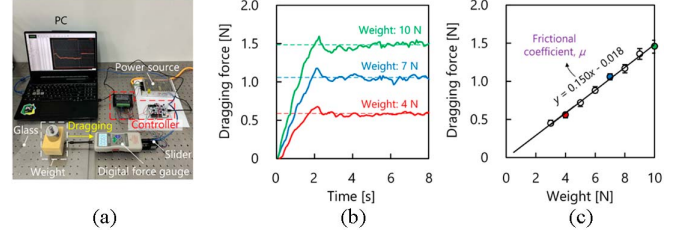


Fig. 12. Measurement of the frictional coefficient. (a) Testbed, (b) variation in the dragging force when the weights of 4, 7, and 10 N are applied, and (c) relationship between the dragging force and the weight. The slope of the fitting line is 0.15, chosen as the frictional coefficient.

and

$$Z_{1i} = \frac{C_{11}^{\frac{1}{2}}\rho_p^{\frac{1}{2}}h}{e_{31}^2w} \cdot \sin\left(2\pi f_i h_c C_{11}^{-\frac{1}{2}}\rho_p^{\frac{1}{2}}\right) \quad (\text{A3})$$

where e_{31} denotes the piezoelectric constant (-6.8 C/m^2) [52] and w is the PZT plate's width. In addition, the clamped capacitance C_{d1} is given as [18], [29]

$$C_{d1} = \frac{2\varepsilon_{33}h_cw}{h} \quad (\text{A4})$$

where ε_{33} is the dielectric constant ($13.01 \times 10^{-9} \text{ F/m}$) [39].

$$\alpha_{1i} = \begin{bmatrix} \cos\left\{(2\pi f_i)^{\frac{1}{2}} \cdot \frac{h_c}{2} \cdot \left[\frac{(48h\rho_p + 12l_c\rho_{AL})}{(4hC_{11} + l_cE_{AL})(l_c + 2h)^2}\right]^{\frac{1}{4}}\right\} & j(2\pi f_i)^{\frac{1}{2}} \frac{(l_c + 2h)^2(4hl_c\rho_p + l_c^2\rho_{AL})}{(4hl_c + l_c^2)} \left[\frac{(48h\rho_p + 12l_c\rho_{AL})}{(4hC_{11} + l_cE_{AL})(l_c + 2h)^2}\right]^{\frac{1}{4}} \\ -j \cdot \sin\left\{(2\pi f_i)^{\frac{1}{2}} \cdot \frac{h_c}{2} \cdot \left[\frac{(48h\rho_p + 12l_c\rho_{AL})}{(4hC_{11} + l_cE_{AL})(l_c + 2h)^2}\right]^{\frac{1}{4}}\right\} & \times \sin\left\{(2\pi f_i)^{\frac{1}{2}} \cdot \frac{h_c}{2} \cdot \left[\frac{(48h\rho_p + 12l_c\rho_{AL})}{(4hC_{11} + l_cE_{AL})(l_c + 2h)^2}\right]^{\frac{1}{4}}\right\} \\ \frac{(2\pi f_i)^{\frac{1}{2}}(l_c + 2h)^2(4hl_c\rho_p + l_c^2\rho_{AL})}{(4hl_c + l_c^2)} \left[\frac{(48h\rho_p + 12l_c\rho_{AL})}{(4hC_{11} + l_cE_{AL})(l_c + 2h)^2}\right]^{\frac{1}{4}} & \cos\left\{(2\pi f_i)^{\frac{1}{2}} \cdot \frac{h_c}{2} \cdot \left[\frac{(48h\rho_p + 12l_c\rho_{AL})}{(4hC_{11} + l_cE_{AL})(l_c + 2h)^2}\right]^{\frac{1}{4}}\right\} \end{bmatrix} \quad (\text{A1})$$

$$\alpha_{2i} = \begin{bmatrix} \cos\left\{(2\pi f_i)^{\frac{1}{2}} \frac{(l - 2h_c)}{2} \left[\frac{(24hl_c + 24h^2)\rho_p}{(3l_c^2h + l_ch^2 + 4h^3)C_{11}}\right]^{\frac{1}{4}}\right\} & j(2\pi f_i)^{\frac{1}{2}}\rho_p(4hl_c + 4h^2) \left\{\frac{[(l_c + 2h)^4 - l_c^4]C_{11}}{12[(l_c + 2h)^2 - l_c^2]\rho_p}\right\}^{\frac{1}{4}} \\ -j \sin\left\{(2\pi f_i)^{\frac{1}{2}} \frac{(l - 2h_c)}{2} \left[\frac{(24hl_c + 24h^2)\rho_p}{(3l_c^2h + l_ch^2 + 4h^3)C_{11}}\right]^{\frac{1}{4}}\right\} & \times \sin\left\{(2\pi f_i)^{\frac{1}{2}} \frac{(l - 2h_c)}{2} \left[\frac{(24hl_c + 24h^2)\rho_p}{(3l_c^2h + l_ch^2 + 4h^3)C_{11}}\right]^{\frac{1}{4}}\right\} \\ \frac{(2\pi f_i)^{\frac{1}{2}}\rho_p(4hl_c + 4h^2) \left\{\frac{[(l_c + 2h)^4 - l_c^4]C_{11}}{12[(l_c + 2h)^2 - l_c^2]\rho_p}\right\}^{\frac{1}{4}}}{(2\pi f_i)^{\frac{1}{2}}\rho_p(4hl_c + 4h^2) \left\{\frac{[(l_c + 2h)^4 - l_c^4]C_{11}}{12[(l_c + 2h)^2 - l_c^2]\rho_p}\right\}^{\frac{1}{4}}} & \cos\left\{(2\pi f_i)^{\frac{1}{2}} \frac{(l - 2h_c)}{2} \left[\frac{(24hl_c + 24h^2)\rho_p}{(3l_c^2h + l_ch^2 + 4h^3)C_{11}}\right]^{\frac{1}{4}}\right\} \end{bmatrix} \quad (\text{A5})$$

$$\gamma_{2i} = \begin{bmatrix} 0 & -j \cdot \frac{h\rho_p^{\frac{1}{2}}C_{11}^{\frac{1}{2}}}{2e_{31}\sin\left[\pi(l - 2h_c)f_i\rho_p^{\frac{1}{2}}C_{11}^{-\frac{1}{2}}\right]} \\ -j \cdot \frac{2e_{31}\sin\left[\pi(l - 2h_c)f_i\rho_p^{\frac{1}{2}}C_{11}^{-\frac{1}{2}}\right]}{h\rho_p^{\frac{1}{2}}C_{11}^{\frac{1}{2}}} & 0 \end{bmatrix} \quad (\text{A6})$$

$$\alpha_{4i} = \begin{bmatrix} \cos \left[(2\pi f_i)^{\frac{1}{2}} l_f \rho_{AL}^{\frac{1}{4}} E_{AL}^{-\frac{1}{4}} \right] & 0.5j(2\pi f_i)^{\frac{1}{2}} \pi d_f^2 E_{AL}^{\frac{1}{4}} \rho_{AL}^{\frac{3}{4}} \sin \left[(2\pi f_i)^{\frac{1}{2}} l_f \rho_{AL}^{\frac{1}{4}} E_{AL}^{-\frac{1}{4}} \right] \\ -2j \sin \left[(2\pi f_i)^{\frac{1}{2}} l_f \rho_{AL}^{\frac{1}{4}} E_{AL}^{-\frac{1}{4}} \right] & \cos \left[(2\pi f_i)^{\frac{1}{2}} l_f \rho_{AL}^{\frac{1}{4}} E_{AL}^{-\frac{1}{4}} \right] \\ \frac{\pi (2\pi f_i)^{\frac{1}{2}} d_f^2 E_{AL}^{\frac{1}{4}} \rho_{AL}^{\frac{3}{4}}}{\pi (2\pi f_i)^{\frac{1}{2}} d_f^2 E_{AL}^{\frac{1}{4}} \rho_{AL}^{\frac{3}{4}}} & \end{bmatrix} \quad (A9)$$

2) *Hollow part.* The matrix α_{2i} is given as [18], [29]

In addition, γ_{2i} , Z_{2i} , and C_{d2} are expressed as [50], [51]

$$Z_{2i} = \frac{\rho_p^{\frac{1}{2}} C_{11}^{\frac{1}{2}} h}{e_{31}^2 w} \cdot \sin \left[2\pi f_i (l - 2h_c) C_{11}^{-\frac{1}{2}} \rho_p^{\frac{1}{2}} \right] \quad (A7)$$

and

$$C_{d2} = \frac{2\varepsilon_{33}(l - 2h_c)w}{h} \quad (A8)$$

respectively.

3) *End connector.* Considering that the dimensions of the end connector are nearly identical with those of the neck connector, we set $\alpha_{3i} = \alpha_{1i}$, $\gamma_{3i} = \gamma_{1i}$, $Z_{3i} = Z_{1i}$, and $C_{d3} = C_{d1}$ [18].

4) *Driving foot.* Each block in the right side contains α_{4i} as the driving foot has the function of propagating the wave [50]. α_{4i} is expressed as [1], [29], [50]

where l_f and d_f are the length and the diameter of the driving foot, respectively.

B. Elements for Analyzing the Friction Property

The elements given in Fig. 3(b) show the friction properties. The mechanical part's weight m_e and the payload m_p are modeled as the inductance [18]. The friction force is estimated with the following [4]:

$$f_{\text{friction}} = \text{sgn}(v_{df} - v_m) \cdot \mu(m_e + m_p)g \quad (A10)$$

where $\text{sgn}()$ is the signum function, v_{df} and v_m are respectively the vibration velocity at the driving foot and the speed of SMPA, g is the gravity unit, and μ is the frictional coefficient, set to 0.15 based on the measurement results. In specific, a digital force gauge (DS2, Zhiqv Precision Instrument Corp., Dongguan, China) was mounted on a slider that dragged SMPA to generate linear movement [Fig. 12(a)], and the results were recorded with a host computer of the force gauge. Meanwhile, the preloads were adjusted by applying different weights to SMPA. Fig. 12(b) plots the dragging force in the time domain when the weights are 4, 7, and 10 N. Fig. 12(c) illustrates the relationship between the dragging force and the weight, where the slope of the fitting line (0.15) is regarded as the frictional coefficient. Besides, the element modeled as a DC voltage source (indicates as $m_{\text{tow}}g$) stands for the towing weight. When analyzing the relationship between m_p and v_m , we set m_{tow} to zero as no weight is towed in this case [53].

REFERENCES

- [1] B. Hao, L. Wang, R. Wang, Y. Sun, J. Jin, and Q. Xu, "Numerical analysis and experimental investigation on a novel piezoelectric actuated rail-type mobile platform," *IEEE/ASME Trans. Mechatron.*, vol. 27, no. 2, pp. 744–752, Apr. 2022.
- [2] D. Berry et al., "Progressing towards high performance non-resonant piezoelectric stepping actuators," *Sens. Actuators A*, vol. 358, Aug. 2023, Art. no. 114439.
- [3] R. Merry et al., "Using a walking piezo actuator to drive and control a high-precision stage," *IEEE/ASME Trans. Mechatron.*, vol. 14, no. 1, pp. 21–31, Feb. 2009.
- [4] W. Qiu et al., "Efficiency improvement of hybrid transducer-type ultrasonic motor using lubricant," *IEEE Trans. Ultrason. Ferroelect. Freq. Control*, vol. 60, no. 4, pp. 786–794, Apr. 2013.
- [5] Z. Xu, W. Sun, X. Li, H. Huang, and J. Dong, "A stick-slip piezoelectric actuator with high assembly interchangeability," *Int. J. Mech. Sci.*, vol. 233, Nov. 2022, Art. no. 107662.
- [6] J. Li, H. Huang, and H. Zhao, "A piezoelectric-driven linear actuator by means of coupling motion," *IEEE Trans. Ind. Electron.*, vol. 65, no. 3, pp. 2458–2466, Mar. 2018.
- [7] J. Sun, D. Zhou, Y. Liu, J. Deng, and S. Zhang, "Development of a minimally invasive surgical robot using self-helix twisted artificial muscles," *IEEE Trans. Ind. Electron.*, vol. 71, no. 2, pp. 1779–1789, Feb. 2024.
- [8] R. Merry et al., "Modeling of a walking piezo actuator," *Sens. Actuator A*, vol. 162, no. 1, pp. 51–60, Jul. 2010.
- [9] S. Tadigadapa, "Piezoelectric microelectromechanical systems—Challenges and opportunities," *Procedia Eng.*, vol. 5, pp. 468–471, Oct. 2010.
- [10] T. Abondance, K. Jayaram, N. T. Jafferis, J. Shum, and R. J. Wood, "Piezoelectric grippers for mobile micromanipulation," *IEEE Robot. Autom. Lett.*, vol. 5, no. 3, pp. 4407–4414, Jul. 2020.
- [11] B. Jia et al., "A novel traveling wave piezoelectric actuated wheeled robot: design, theoretical analysis, and experimental investigation," *Smart Mater. Struct.*, vol. 30, no. 3, Feb. 2021, Art. no. 035016.
- [12] W. Wang, J. Deng, Y. Liu, S. Zhang, J. Li, and X. Gao, "Design, modeling and experiment of a miniature biped piezoelectric robot," *Smart Mater. Struct.*, vol. 31, no. 7, May 2022, Art. no. 075004.
- [13] J. Deng, W. Chen, K. Li, L. Wang, and Y. Liu, "A sandwich piezoelectric actuator with long stroke and nanometer resolution by the hybrid of two actuation modes," *Sens. Actuator A*, vol. 296, pp. 121–131, Sep. 2019.
- [14] J. Li, J. Deng, S. Zhang, and Y. Liu, "Development of a miniature quadrupedal piezoelectric robot combining fast speed and nano-resolution," *Int. J. Mech. Sci.*, vol. 250, Jul. 2023, Art. no. 108276.
- [15] K. Jayaram, J. Shum, S. Castellanos, E. F. Helbling, and R. J. Wood, "Scaling down an insect-size microrobot, HAMR-VI into HAMR-Jr," in *Proc. IEEE Int. Conf. Robot. Automat.*, May 2020, pp. 10305–10311.
- [16] E. Zhang, Y. Hu, H. Bao, J. Li, J. Ma, and J. Wen, "A linear inertial piezoelectric actuator using a single bimorph vibrator," *Smart Mater. Struct.*, vol. 28, no. 11, Oct. 2019, Art. no. 115020.
- [17] J. Li et al., "An untethered tripodal miniature piezoelectric robot with strong load capacity inspired by land motion of seals," *IEEE/ASME Trans. Mechatron.*, vol. 29, no. 1, pp. 85–96, Feb. 2024, doi: 10.1109/TMECH.2023.3269014.
- [18] J. Wu et al., "Development of a self-moving ultrasonic actuator with high carrying/towing capability driven by longitudinal traveling wave," *IEEE/ASME Trans. Mechatron.*, vol. 28, no. 1, pp. 267–279, Oct. 2022.
- [19] J. Li, J. Deng, Y. Liu, S. Zhang, and K. Li, "Development of a planar tripodal piezoelectric robot with a compact ring structure," *IEEE/ASME Trans. Mechatron.*, vol. 27, no. 5, pp. 3908–3919, Oct. 2022.
- [20] C. Guan and Z. Jiao, "A piezoelectric direct-drive servo valve with a novel multi-body contacting spool-driving mechanism: design, modelling and experiment," *Proc. Inst. Mech. Eng.*, vol. 228, no. 1, pp. 169–185, Jan. 2014.
- [21] S. Ghenna, Y. Bernard, and L. Daniel, "Design and experimental analysis of a high force piezoelectric linear motor," *Mechatronics*, vol. 89, Feb. 2023, Art. no. 102928.
- [22] M. Hunstig, T. Hemsell, and W. Sextro, "Stick-slip and slip-slip operation of piezoelectric inertia drives. Part I: Ideal excitation," *Sens. Actuator A*, vol. 200, pp. 90–100, Oct. 2013.

- [23] X. M. Y. Liu, J. Liu, and J. Deng, "Crabbot: A pole-climbing robot driven by piezoelectric stack," *IEEE Trans. Robot.*, vol. 38, no. 2, pp. 765–778, Apr. 2022.
- [24] J. Deng et al., "Design and experiments of a small resonant inchworm piezoelectric robot," *Sci. China Technol. Sci.*, vol. 66, no. 3, pp. 821–829, Mar. 2023.
- [25] H. Yu, Y. Liu, J. Deng, S. Zhang, and W. Chen, "A collaborative excitation method for piezoelectric stick-slip actuator to eliminate rollback and generate precise smooth motion," *Mech. Syst. Signal Process.*, vol. 170, May 2022, Art. no. 108815.
- [26] K. Wang et al., "A novel piezoelectric linear actuator designed by imitating skateboarding movement," *Smart Mater. Struct.*, vol. 29, no. 11, Oct. 2020, Art. no. 115038.
- [27] J. Li et al., "A bionic type piezoelectric actuator based on walking motion and asymmetrical L-shaped flexure mechanisms," *IEEE/ASME Trans. Mechatron.*, vol. 28, no. 3, pp. 1326–1336, Jun. 2023.
- [28] B. Shi et al., "Design of a rhombus-type stick-slip actuator with two driving modes for micro-positioning," *Mech. Syst. Signal Process.*, vol. 166, Mar. 2022, Art. no. 108421.
- [29] W. Wei et al., "A miniature piezoelectric actuator with fast movement and nanometer resolution," *Int. J. Mech. Sci.*, vol. 273, Jul. 2024, Art. no. 109249.
- [30] K.-B. Choi, J. J. Lee, G. H. Kim, and H. J. Lim, "A compliant parallel mechanism with flexure-based joint chains for two translations," *Int. J. Precis. Eng. Manuf.*, vol. 13, no. 9, pp. 1625–1632, Sep. 2012.
- [31] G. Qiao, H. Li, X. Lu, J. Wen, and T. Cheng, "Piezoelectric stick-slip actuators with flexure hinge mechanisms: A review," *J. Intell. Mater. Syst. Struct.*, vol. 33, no. 15, pp. 1879–1901, Sep. 2022.
- [32] J. Li, B. Xu, J. Deng, W. Chen, and Y. Liu, "Development of a miniature piezoelectric robot combining three unconventional inertial impact modes," *Sens. Actuator A*, vol. 365, Jan. 2024, Art. no. 114898.
- [33] H. Huang et al., "Achieving stable and effective stick-slip motions of piezoelectric actuators with a small mass rotor by means of the auxiliary friction," *IEEE Trans. Ind. Electron.*, in press. doi: 10.1109/TIE.2024.3355497.
- [34] H. H. Hariri et al., "A tether-less legged piezoelectric miniature robot using bounding gait locomotion for bidirectional motion," in *Proc. IEEE Inter. Conf. Robot. Automat.*, May 2016, pp. 4743–4749.
- [35] T. Morita, H. Murakami, T. Yokose, and H. Hosaka, "A miniaturized resonant-type smooth impact drive mechanism actuator," *Sens. Actuators A*, vol. 178, pp. 188–192, May 2012.
- [36] F. Wang et al., "Dynamic resonance frequency control for a resonant-type smooth impact drive mechanism actuator," *Sens. Actuator A*, vol. 359, Sep. 2023, Art. no. 114462.
- [37] S. Mohith et al., "Recent trends in piezoelectric actuators for precision motion and their applications: A review," *Smart Mater. Struct.*, vol. 30, no. 1, Dec. 2020, Art. no. 013002.
- [38] J. Wu et al., "A two-DOF linear ultrasonic motor with high thrust force density and high power density utilizing torsional/centrosymmetric-bending/symmetric-bending modes," *IEEE Trans. Ind. Electron.*, vol. 69, no. 8, pp. 8220–8230, Aug. 2022.
- [39] L. Wang et al., "A millipede-inspired miniature self-moving ultrasonic actuator with high carrying capability and nanometer resolution," *Int. J. Mech. Sci.*, vol. 267, Apr. 2024, Art. no. 109017.
- [40] M. Majidi et al., "A multi-objective model for optimal operation of a battery/PV/fuel cell/grid hybrid energy system using weighted sum technique and fuzzy satisfying approach considering responsible load management," *Sol. Energy*, vol. 144, pp. 79–89, Mar. 2017.
- [41] A. Makishima and J. Mackenzie, "Calculation of bulk modulus, shear modulus and Poisson's ratio of glass," *J. Non-Cryst. Solids*, vol. 17, no. 2, pp. 147–157, Mar. 1975.
- [42] N. Matuda, S. Baba, and A. Kinbara, "Internal stress, young's modulus and adhesion energy of carbon films on glass substrates," *Thin Solid Films*, vol. 81, no. 4, pp. 301–305, Jul. 1981.
- [43] Y. Wang et al., "A resonant-type thin plate piezoelectric actuator inspired by koala's locomotion," *IEEE Trans. Ind. Electron.*, vol. 70, no. 8, pp. 8235–8243, Aug. 2023.
- [44] H. Hariri, Y. Bernard, and A. Razek, "2-D traveling wave driven piezoelectric plate robot for planar motion," *IEEE/ASME Trans. Mechatron.*, vol. 23, no. 1, pp. 242–251, Feb. 2018.
- [45] J. Liu, J. Wu, X. Gao, Z. Ding, and W. Wei, "Enhancement of torque density and power density of polymer-based ultrasonic motors via flexible usage of anisotropy in elastic property," *Smart Mater. Struct.*, vol. 32, no. 7, Jun. 2023, Art. no. 075020.
- [46] J. Wu, Y. Mizuno, and K. Nakamura, "Polymer-based ultrasonic motors utilizing high-order vibration modes," *IEEE/ASME Trans. Mechatron.*, vol. 23, no. 2, pp. 788–799, Apr. 2018.
- [47] S. Liu et al., "Contact force/motion hybrid control for a hydraulic legged mobile manipulator via a force-controlled floating base," *IEEE/ASME Trans. Mechatron.*, in press. doi: 10.1109/TMECH.2023.3323541.
- [48] Y. Liu et al., "S2worm: A fast-moving untethered insect-scale robot with 2-DOF transmission mechanism," *IEEE Robot. Autom. Lett.*, vol. 7, no. 3, pp. 6758–6765, Jul. 2022.
- [49] C. Naab and Z. Zheng, "Application of the unscented Kalman filter in position estimation a case study on a robot for precise positioning," *Robot. Auton. Syst.*, vol. 147, Jan. 2022, Art. no. 103904.
- [50] R. Krimholtz, D. A. Leedom, and G. L. Matthaei, "New equivalent circuits for elementary piezoelectric transducers," *Electron. Lett.*, vol. 6, no. 13, pp. 398–399, 1970.
- [51] L. Wang et al., "Development of a compact and contactless stage capable of levitating/rotating wafer functioning as an ultrasonically virtual hand," *IEEE Trans. Ind. Electron.*, early access, doi: 10.1109/TIE.2024.3363721.
- [52] J. Southin, S. Wilson, D. Schmitt, and R. Whatmore, "e31, f determination for PZT films using a conventional 'd33' meter," *J. Phys. D: Appl. Phys.*, vol. 34, pp. 1456–1460, Jan. 2001.
- [53] K. Nakamura, "Evaluation methods for materials for power ultrasonic applications," *Jpn. J. Appl. Phys.*, vol. 59, Jun. 2020, Art. no. SK0801.



Jinshuo Liu was born in Shandong, China, in 2001. He is currently working toward the bachelor's degree with the School of Control Science and Technology, Shandong University, Jinan, China.

His research interests include piezoelectric actuation and its application to precise manipulation/operation.



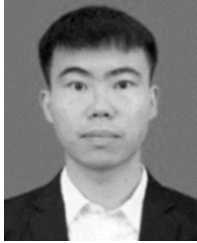
Zhaochun Ding was born in Shandong, China, in 2001. He received the bachelor's degree in mechanical engineering in 2023, from Shandong University, Jinan, China, where he is working toward the master's degree in control science and technology.

His research interest includes piezoelectric actuation and its application to miniature robots.



Jiang Wu was born in Liaoning, China, in 1988. He received the B.E. degree in mechanical engineering from Dalian University of Technology, Dalian, China, in 2010, the M.E. degree in mechatronic engineering from the State Key Laboratory of Robotics and System, Harbin Institute of Technology, Harbin, China, in 2012, and the Ph.D. degree in electric and electronic engineering from the Future Interdisciplinary Research of Science and Technology, Tokyo Institute of Technology, Yokohama, Japan, in 2017.

He is currently a Professor with the School of Control Science and Technology, Shandong University, Jinan, China, where he is active in developing ultrasonically levitating devices and piezoelectric actuators/robots.



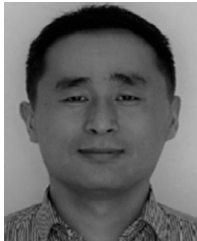
Lipeng Wang received the B.S. and M.S. degrees in mechanical engineering from Yan-shan University, Qinhuangdao, China, in 2018 and 2022, respectively. He is currently working toward the Ph.D. degree with the School of Control Science and Technology, Shandong University, Jinan, China.

His research interests include ultrasonic levitation-based devices and piezoelectric actuation.



Teng Chen received the bachelor's degree in automation and Ph.D. degree in pattern recognition and intelligent system from Shandong University, Jinan, China, in 2015 and 2020, respectively.

He is currently an Lab Master with the School of Control Science and Engineering, Shandong University. His research interests include bionic robotics, control system, and reinforcement learning.



Xuewen Rong received the B.S. degree in mechanical design and manufacturing and M.S. degree in control science and engineering from Shandong University of Science and Technology, Jinan, China, in 1996 and 1999, respectively, and the Ph.D. degree in control science and engineering from Shandong University, Jinan, China, in 2013.

He is currently a Professor with the School of Control Science and Technology, Shandong University. His research interests include bionic

robotics, mechatronics, hydraulic servo transmission, and control systems.



Rui Song (Member, IEEE) received the B.S. degree in industrial automation and the M.S. degree in control theory and engineering from Shandong University of Science and Technology, Jinan, China, in 1998 and 2001, respectively, and the Ph.D. degree in control theory and engineering from Shandong University, Jinan, China, in 2011.

He is currently a Professor with the School of Control Science and Technology, Shandong University. His research interests include intelli-

gent bionic robots, control theory and application, and automation engineering.



Yibin Li received the B.S. degree in automation engineering from Tianjin University, Tianjin, China, in 1982, the M.S. degree in electrical engineering from Shandong University of Science and Technology, Jinan, China, in 1990, and the Ph.D. degree in automation engineering from Tianjin University, in 2008.

He is currently a Professor with the School of Control Science and Engineering, Shandong University, Jinan, China. His research interests include intelligent robots, special robots, intelli-

gent vehicles, intelligent control, and mechatronics.